Photodissociation dynamics of the singlet and triplet states of the NCN radical

Ryan T. Bise, Hyeon Choi, and Daniel M. Neumark[a)]
Department of Chemistry, University of California, Berkeley, California 94720 and Chemical Sciences Division, Lawrence Berkeley National Laboratories, Berkeley, California 94720

The spectroscopy and photodissociation dynamics of the NCN radical have been investigated by fast beam photofragment translational spectroscopy. The $\widetilde{B}\,^3\Sigma_u^-\leftarrow\widetilde{X}\,^3\Sigma_g^-$, $\widetilde{c}\,^1\Pi_u\leftarrow\widetilde{a}\,^1\Delta_g$, and $\widetilde{d}\,^1\Delta_u\leftarrow\widetilde{a}\,^1\Delta_g$ transitions were examined. The major dissociation products for the $\widetilde{B}\,^3\Sigma_u^-$ and $\widetilde{c}\,^1\Pi_u$ states are $N_2(\widetilde{X}\,^1\Sigma_g^+)+C(^3P)$, while the $\widetilde{d}\,^1\Delta_u$ state dissociates to $N_2(\widetilde{X}\,^1\Sigma_g^+)+C(^1D)$. The dissociation channel, $N(^4S)+CN(\widetilde{X}\,^2\Sigma^+)$ is observed for the $\widetilde{B}\,^3\Sigma_u^-$ state at photon energies greater than 4.9 eV, where it comprises $\approx 25\pm 10\%$ of the total signal. At all photon energies, the photofragment translational energy distributions show a resolved progression corresponding to the vibrational excitation of the N_2 photofragment. The rotational distributions of the molecular fragments suggest that the dissociation pathway for the N_2 loss channel involves a bent transition state while the N+CN photofragments are produced via a linear dissociation mechanism. The $P(E_T)$ distributions provide bond dissociation energies of 2.54 ± 0.030 and 4.56 ± 0.040 eV for the N_2 and CN loss channels, respectively, yielding $\Delta H_{f,0\,K}(NCN)=4.83\pm 0.030$ eV. © *1999 American Institute of Physics.* [S0021-9606(99)00535-8]

I. INTRODUCTION

Photodissociation of small polyatomic molecules provides a rich probe of the potential energy surfaces involved in bond rupture. Detailed measurements such as photofragment yield spectra, translational energy distributions, and product branching ratios allow for a careful examination of the dissociation mechanism.[1] While there have been numerous photodissociation studies of stable closed-shell molecules, far fewer studies of open-shell radicals have been performed. Our laboratory has demonstrated the ability to generate a well-characterized source of radicals via photodetachment of negative ions, allowing us to perform photodissociation experiments on reactive open-shell species. Here, we report the photodissociation dynamics for triplet and singlet electronic states of the NCN radical.

The NCN free radical has been proposed as an important combustion intermediate since its emission was observed in hydrocarbon flames by Jennings and Linnett.[2] It has been suggested by Smith *et al.*[3] that the NCN radical plays a significant role in the combustion of nitramine propellant molecules, given the large extent of C–N bonding in these molecules. Additionally, ultraviolet emission studies of the comet Brorosen–Metcalf suggest that NCN is present in comets and is a source of CN radicals.[4]

The NCN radical has attracted a great deal of attention from both spectroscopists and theorists who have been particularly concerned with its bonding and geometry. The ground and relevant excited states for this study are shown in Fig. 1 with the corresponding dominant electronic configurations given below:

$$...(3\sigma_u)^2(1\pi_u)^4(1\pi_g)^2 \quad \widetilde{X}\,^3\Sigma_g^-,\widetilde{a}\,^1\Delta_g,\widetilde{b}\,^1\Sigma_g^+$$

$$...(3\sigma_u)^1(1\pi_u)^4(1\pi_g)^3 \quad \widetilde{A}\,^3\Pi_u,\widetilde{c}\,^1\Pi_u$$

$$...(3\sigma_u)^2(1\pi_u)^3(1\pi_g)^3 \quad \widetilde{B}\,^3\Sigma_u^-,\widetilde{d}\,^1\Delta_u.$$

According to Walsh's rules,[5] all of these electronic states are predicted to be linear.

Rotationally resolved ultraviolet absorption spectra were measured by Travis and Herzberg[6] for the $\widetilde{A}\,^3\Pi_u\leftarrow\widetilde{X}\,^3\Sigma_g$ band, and by Kroto[7,8] for the $\widetilde{c}\,^1\Pi_u\leftarrow\widetilde{a}\,^1\Delta_g$ band, confirming that these states are linear. Kroto observed a number of higher lying transitions attributed to the $\widetilde{B}\,^3\Sigma_u^-\leftarrow\widetilde{X}\,^3\Sigma_g^-$ and $\widetilde{d}\,^1\Delta_u\leftarrow\widetilde{a}\,^1\Delta_g$ bands.[9] Milligan, Jacox, and Bass observed this $\widetilde{B}\,^3\Sigma_u^-\leftarrow\widetilde{X}\,^3\Sigma_g^-$ band as well as a number of infrared absorptions in matrix isolation studies.[10,11]

In the matrix work, depletion of the NCN radical was observed at wavelengths shorter than 280 nm (4.42 eV); on the basis of secondary reaction products within the matrix, the authors proposed that NCN dissociates to $N_2(\widetilde{X}\,^1\Sigma_g^+)+C(^3P)$ in this wavelength range, which overlaps the $\widetilde{B}\,^3\Sigma_u^-\leftarrow\widetilde{X}\,^3\Sigma_g^-$ band. Smith *et al.*[3] measured the radiative lifetime for the vibrationless level and a number of vibronic bands of the $\widetilde{A}\,^3\Pi_u$ state, determining the radiative lifetime of the vibrationless level to be 183 ns. The radiative lifetimes show very little variation with increased vibrational excitation, implying that this state does not dissociate.

More recently, McNaughton and co-workers[12] measured a high resolution Fourier transform infrared spectrum of the NCN antisymmetric stretch band in the gas phase. Brown
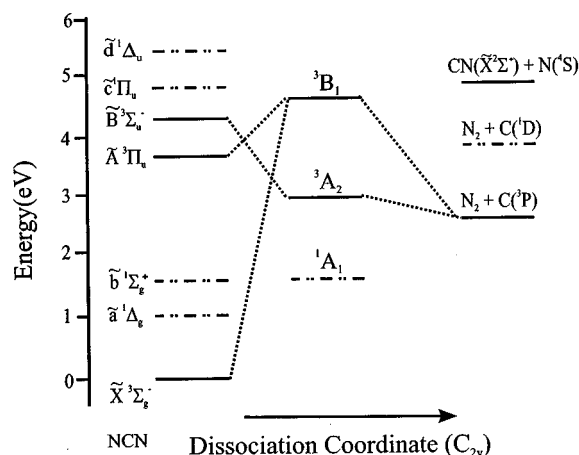
FIG. 1. Energy level and correlation diagram for the NCN radical along a C_{2v} dissociation coordinate. The energies of the $\tilde{a}\,^1\Delta_g$, $\tilde{b}\,^1\Sigma_g^+$, $\tilde{A}\,^3\Pi_u$, $\tilde{B}\,^3\Sigma_u^-$, $\tilde{c}\,^1\Pi_u$, and $\tilde{d}\,^1\Delta_u$ states are based upon experimental work discussed in the text. The $^1A_1$, $^3A_2$, and $^3B_2$ states are from *ab initio* calculations (Ref. 24) and the product state energies are from JANAF thermochemical tables (Ref. 42).
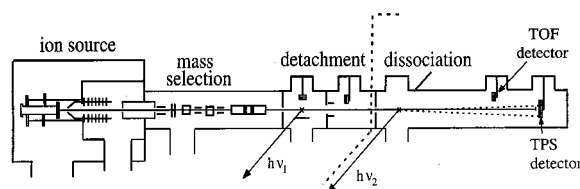

FIG. 2. Fast radical beam translational spectrometer. The dotted line separates the radical production section on the left from the photodissociation experiment on the right.

and co-workers[13–16] used laser-induced fluorescence and laser magnetic resonance to refine the spectroscopic constants of the $\tilde{X}$ and $\tilde{A}$ states and obtain estimates of the bend frequencies in the two states.

The photoelectron spectrum of NCN$^-$ measured by Clifford *et al.*[17] showed the photodetachment process to be vertical, giving rise to no vibrational excitation of the neutral radical upon photodetachment. Higher energy photoelectron spectroscopy studies performed by Taylor *et al.*[18] located the $\tilde{a}\,^1\Delta_g$ and $\tilde{b}\,^1\Sigma_g^+$ states relative to the $\tilde{X}\,^3\Sigma_g^-$ ground state, thereby determining the singlet–triplet splitting, $E(\tilde{a}\,^1\Delta_g - \tilde{X}\,^3\Sigma_g^-) = 1.010 \pm 0.010\,\text{eV}$.

Theoretical studies of the geometry and bonding of the NCN radical showed the ground state to be linear with the central carbon doubly bonded to both nitrogen atoms.[17,19–23] Martin *et al.* have performed *ab initio* studies on both the NCN and CNN radicals for linear, cyclic, and bent geometries[24] finding the barrier to isomerization to lie approximately 3 eV above the NCN ground state. This is consistent with the experimental observation of both isomers as distinct species.[25–30]

The NCN radical provides as rich system for photodissociation studies. It has several low-lying singlet and triplet excited states above the dissociation limit as well as multiple energetically accessible product states, as shown in Fig. 1. Furthermore, the photodecomposition of NCN to products $N_2 + C(^3P)$ from the linear $\tilde{B}\,^3\Sigma_u^- \leftarrow \tilde{X}\,^3\Sigma_g^-$ transition observed by Milligan and co-workers[10] implies that the dissociation mechanism is complex, possibly involving bent or cyclic electronic states.

In this study, a mass selected beam of NCN radicals is generated from the photodetachment of NCN$^-$ ions and subsequently photodissociated. We recently demonstrated the ability to probe transitions not only from the ground electronic state but also from low-lying excited states of different spin multiplicity.[31] A photodetachment energy slightly above the electron affinity produces the NCN radical in the ground $\tilde{X}\,^3\Sigma_g^-$ state exclusively, allowing us to examine the spectroscopy and dynamics of triplet dissociative electronic states. A higher photodetachment energy can then be used to populate both the $\tilde{X}\,^3\Sigma_g^-$ and $\tilde{a}\,^1\Delta_g$ states, the latter providing access to the dissociative states in the singlet manifold. Overall, we have examined the photodissociation dynamics of the $\tilde{B}\,^3\Sigma_u^- \leftarrow \tilde{X}\,^3\Sigma_g^-$, $\tilde{c}\,^1\Pi_u \leftarrow \tilde{a}\,^1\Delta_g$, and $\tilde{d}\,^1\Delta_u \leftarrow \tilde{a}\,^1\Delta_g$ electronic bands obtaining structured photodissociation cross-sections, product branching ratios, and detailed internal energy distributions of the photofragments.

II. EXPERIMENT

The fast beam photofragment translational spectrometer, Fig. 2, has been described in detail elsewhere;[32–34] only a brief description will follow. In this experiment, we generate a clean source of neutral radicals by mass-selectively photodetaching a beam of stable negative ions. The neutral radicals are then photodissociated by a second laser.

To generate a sufficient number density of NCN$^-$ ions, we made a slight modification to our pulsed electric discharge source[35] by inserting a reservoir containing cyanamide (H$_2$NCN) between the pulsed molecular beam valve and the pulsed electric discharge. Our adaptation of this source has been described in detail previously.[18] Neat O$_2$ at a stagnation pressure of $\sim$3 atm is expanded through a pulsed molecular beam valve into the reservoir containing the cyanamide and finally through the discharge, generating CN$^-$, NCN$^-$, HNCN$^-$, and NCO$^-$ ions. Analysis of photofragment yield spectra obtained in this study indicates that this source produces anions with rotational and vibrational temperatures of 50 and 200 K, respectively.

The negative ions generated in the source region are accelerated to 8 keV and separated temporally by a Bakker time-of-flight (TOF) mass spectrometer, which induces very little kinetic energy spread of the ions.[36,37] The ion of interest is selectively photodetached by a pulsed laser. Based upon the photoelectron spectrum of Taylor *et al.*,[18] an excimer-pumped dye laser operating at 2.82 eV was used to photodetach NCN$^-$ to produce the neutral $\tilde{X}\,^3\Sigma_g^-$ state exclusively, while 4.03 eV light (308 nm) from a XeCl excimer laser was used to populate both the $\tilde{a}\,^1\Delta_g$ and $\tilde{X}\,^3\Sigma_g^-$ states of the neutral. Any undetached ions are deflected out of the beam path.

In the dissociation region, the neutrals are intersected by the frequency-doubled output of an excimer-pumped dye la-

J. Chem. Phys., Vol. 111, No. 11, 15 September 1999

Photodissociation dynamics of NCN   4925

ser with a bandwidth of 0.3 cm^{-1}. A fraction of the neutrals absorb and dissociate yielding photofragments detected directly by either the TOF or TPS (time and position sensing) microchannel plate detector assemblies in Fig. 2. An aluminum strip is positioned at the center of each detector to prohibit any undissociated radicals from impacting the detector, so that any observed signal is entirely from the recoiling photofragments.

Two types of experiments are performed. First, the spectroscopy of the dissociative electronic states is examined by measuring the total flux of photofragments arriving at the retractable TOF detector, located at 0.68 m from the dissociation laser, as a function of photon energy. The resulting photofragment yield (PFY) spectra is complementary to absorption and fluorescence measurements. The current study examined the photolysis of NCN between 30 000 to 43 500 cm^{-1}.

Once the spectroscopy of the dissociative states has been examined, a second type of experiment, which probes the dissociation dynamics, can be performed. In this detection scheme, both photofragments from a single parent radical are detected in coincidence using a time-and-position sensitive (TPS) detector of the type developed by de Bruijn and Los.[38] Our implementation of this detection scheme has been described in detail elsewhere.[32,33] The TPS detector records the positions and difference in arrival time of the two photofragments from a single dissociation event. This information is then used to determine the masses of the fragments, their relative translational energy E_T, and the scattering angle θ between the relative velocity vector and the electric vector of the polarized dissociation laser (parallel to the ion beam axis). The photofragment mass resolution is $m/\Delta m \approx 10$ while the translational energy resolution for these experiments is $\Delta E_T/E_T = 3.0\%$.

Due to the geometry of the TPS detector, which is 40 mm in diameter with an 8 mm beam block located at the center, the detection efficiency of photofragments depends upon their values of θ and E_T. The beam block, in addition to blocking undissociated radicals, prevents fragments of low translational energy or with values of θ close to 0° to 180°
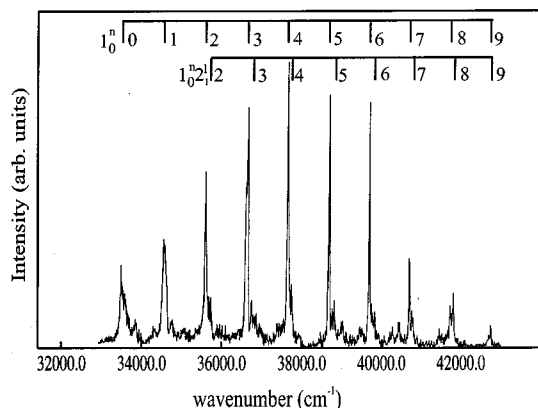
TABLE I. Peak energies, assignments, progression spacings, and widths for the observed transitions in the $\tilde{B}\,^3\Sigma_u^- \leftarrow \tilde{X}\,^3\Sigma_g^-$ PFY spectrum.

Transition energy (cm^{-1})	Assignment	$v(n)-v(n-1)$ (cm^{-1})	FWHM (cm^{-1})
33 488	0_0^0		168
34 555	1_0^1	1067	116
35 597	1_0^2	1042	48
35 714	$2_1^1 1_0^2$		
36 634	1_0^3	1037	86
36 738	$2_1^1 1_0^3$	1024	
37 657	1_0^4	1023	40
37 740	$2_1^1 1_0^4$	1002	
38 654	1_0^5	997	30
38 759	$2_1^1 1_0^5$	1019	
39 698	1_0^6	1044	21
39 774	$2_1^1 1_0^6$	1015	
40 707	1_0^7	1009	20
40 793	$2_1^1 1_0^7$	1019	
41 762	1_0^8	1055	⋯
41 801	$2_1^1 1_0^8$	1008	
42 736	1_0^9	974	20

from reaching the detector, while high-energy recoil fragments with values of θ close to 90° miss the detector. The raw translation energy distributions are therefore normalized by the calculated detector acceptance function, $D(E_T,\theta)$, which has been described in detail by Continetti et al.[39]

III. RESULTS

A. Photofragment yield spectra $\tilde{B}\,^3\Sigma_u^- \leftarrow \tilde{X}\,^3\Sigma_g^-$ transitions

The PFY signal for the $\tilde{B}\,^3\Sigma_u^- \leftarrow \tilde{X}\,^3\Sigma_g^-$ band is shown in Fig. 3, covering 33 000 to 43 000 cm^{-1}. The spectrum shows a progression of predissociative resonances spaced by approximately 1050 cm^{-1}. The positions, assignments, and widths of these transitions are listed in Table I. This progression was observed previously in the ultraviolet absorption studies of Kroto[9] in the gas phase, and by Milligan, Jacox, and Bass[10] in matrix isolation studies, and was assigned to the symmetric stretch (1_0^n) progression. The extended progression and change in frequency from 1259 cm^{-1} in the ground state[40] to 1050 cm^{-1} for the excited state is consistent with promotion of an electron from the $1\pi_u$ to the $1\pi_g$ orbital.

A weaker 1050 cm^{-1} progression is observed ≈ 100 cm^{-1} to the blue of the 1_0^n progression. Travis and Herzberg[6] have shown for second row triatomics that the bending fre-

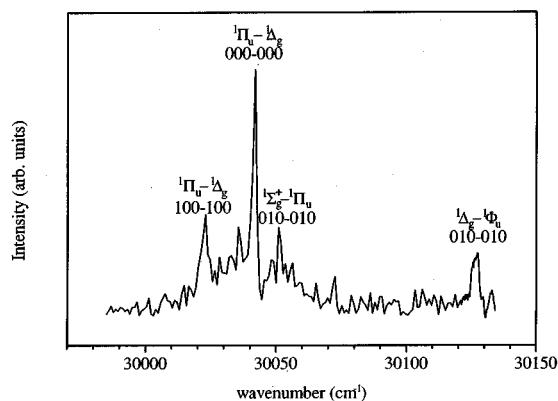FIG. 3. Photofragment yield spectrum of the $\tilde{B}\,^3\Sigma_u^- \leftarrow \tilde{X}\,^3\Sigma_g^-$ band obtained at a photodetachment energy of 2.82 eV. The vibrational combs denote symmetric stretch 1_0^n and sequence band $1_0^n 2_1^1$ progressions.

FIG. 4. Photofragment yield (PFY) spectrum of the $\tilde{c}\,^1\Pi_u \leftarrow \tilde{a}\,^1\Delta_g$ origin band.

FIG. 5. PFY spectrum from 36 300 to 37 800 cm^{-1}. The dashed line indicates features observed at a photodetachment energy of 2.82 eV. The solid line denotes additional features seen at a photodetachment energy of 4.03 eV. These features **a**, **b**, and **c** are assigned to the $\tilde{d}\,^1\Delta_u \leftarrow \tilde{a}\,^1\Delta_g$ band.

quency increases with the number of electrons in the π_g orbital. The bending frequency of the $\tilde{A}\,^3\Pi_u$ state, which also has three electrons in the outermost π_g orbital, was found to be 96 cm^{-1} larger than the ground state bend frequency, estimated to be 437.7 cm^{-1}.[14] On this basis, we assign this progression to the $1_0^n 2_1^1$ sequence band and estimate the bend frequency of the $\tilde{B}\,^3\Sigma_u^-$ state to be 540 ± 20 cm^{-1}.

Neither our photodissociation studies nor the previously mentioned absorption studies have been able to locate any transitions of the $\tilde{B}\,^3\Sigma_u^- \leftarrow \tilde{X}\,^3\Sigma_g^-$ band below the apparent origin at 33 488 cm^{-1}. In agreement with the observations of Kroto,[9] the two lowest energy peaks were found to be remarkably broad, ~ 168 and 116 cm^{-1} in width. The peak widths gradually narrow as the photon energy is increased. The 1_0^3 transition is anomalously broad showing essentially three peaks with the most intense feature located to the blue.

Although we performed scans with a laser bandwidth of 0.2 cm^{-1} and a step size of 0.1 cm^{-1}, we were unable to resolve any rotational structure for the $\tilde{B} \leftarrow \tilde{X}$ band and therefore cannot determine the excited state lifetime from linewidth measurements. The relative intensities of the vibrational features in the PFY spectra are similar to those for the matrix absorption experiments of Milligan et al.,[10] suggesting that the quantum yield for photodissociation is ≈ 1.

Despite extensive efforts to observe the $\tilde{A}\,^3\Pi_u \leftarrow \tilde{X}\,^3\Sigma_g$ transitions, we were unable to detect photodissociation signal from the origin or higher energy vibronic transitions associated with this band.

B. Photofragment yield spectra, $\tilde{c}\,^1\Pi_u \leftarrow \tilde{a}\,^1\Delta_g$ and $\tilde{d}\,^1\Delta_u \leftarrow \tilde{a}\,^1\Delta_g$ transitions

Figure 4 shows the PFY spectrum from 30 000 to 30 150 cm^{-1} when the photodetachment energy is 4.03 eV. The recent photoelectron spectrum taken by Taylor et al.[18] showed that a photodetachment energy of 4.03 eV will populate both the $\tilde{X}\,^3\Sigma_g^-$ and $\tilde{a}\,^1\Delta_g$ electronic states with an intensity ratio of approximately 2:1. Since the anion and neutral have essentially the same geometry, photodetachment of NCN$^-$
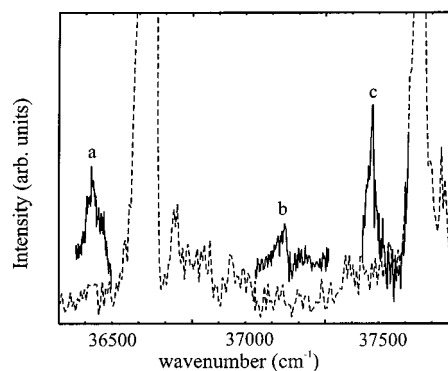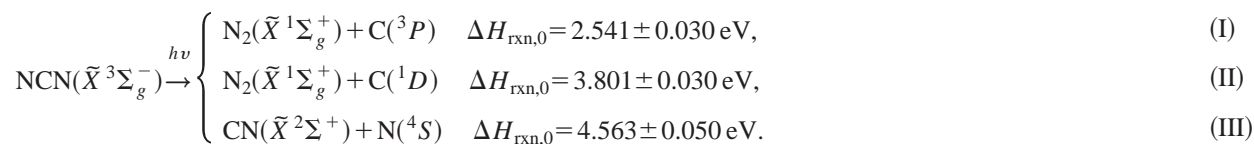
yields minimal vibrational excitation of the neutral radical, allowing the anion to be photodetached well above threshold while maintaining a cold neutral vibrational distribution. Any new features in the PFY spectrum are therefore a result of transitions from the $\tilde{a}\,^1\Delta_g$ electronic state.

The intense transition centered around 30 045 cm^{-1} agrees well with the rotationally resolved spectrum obtained by Kroto,[7] which he assigns to the (000–000) transition of the $\tilde{c}\,^1\Pi_u \leftarrow \tilde{a}\,^1\Delta_g$ band. Additional weaker features seen at 30 025, 30 045, and 30 130 cm^{-1} are consistent with bandheads observed by Kroto and are assigned to the (100–100) $^1\Pi_u \leftarrow {}^1\Delta_g$, (010–010) $^1\Sigma_g^+ \leftarrow {}^1\Pi_u$, and (010–010) $^1\Delta_g \leftarrow {}^1\Phi_u$ vibronic transitions, respectively. The rotational contour of the (000–000) band is characteristic of a perpendicular transition moment with an intense Q-branch and weaker P- and R-branches. The Q-branches of the (100–100) $^1\Pi_u \leftarrow {}^1\Delta_g$ and (010–010) $^1\Sigma_g^+ \leftarrow {}^1\Pi_u$ bands are heavily overlapped by the P- and R-branches of the (000–000) transition, respectively. Using the previously determined rotational constants, the best fit to this rotational contour is achieved with a rotational temperature of 50 K.

Figure 5 shows the PFY spectrum for the wavelength region between 36 200 to 37 800 cm^{-1} obtained at 4.03 eV photodetachment energy. In addition to the $\tilde{B}\,^3\Sigma_u^- \leftarrow \tilde{X}\,^3\Sigma_g^-$ transitions seen in Fig. 3, a number of new transitions appear labeled **a**, **b**, and **c**. These transitions have been observed previously in the gas phase absorption studies of Kroto and co-workers[9] and were assigned to the $\tilde{d}\,^1\Delta_u \leftarrow \tilde{a}\,^1\Delta_g$ band based on kinetic information and complicated vibrational structure. The most intense features, **a** and **c**, belong to a progression of ≈ 1020 cm^{-1} which is attributed to the symmetric stretch. The weaker feature **b** most likely involves bend excitation. Our photodetachment technique confirms that these transitions originate from the $\tilde{a}\,^1\Delta_g$ state.

C. Translational energy distributions

At the photon energies explored in this study, three possible dissociation channels are accessible:

$$\text{NCN}(\widetilde{X}\,^3\Sigma_g^-) \xrightarrow{h\nu} \begin{cases} \text{N}_2(\widetilde{X}\,^1\Sigma_g^+) + \text{C}(^3P) & \Delta H_{\text{rxn,0}} = 2.541 \pm 0.030\,\text{eV}, \quad (\text{I}) \\ \text{N}_2(\widetilde{X}\,^1\Sigma_g^+) + \text{C}(^1D) & \Delta H_{\text{rxn,0}} = 3.801 \pm 0.030\,\text{eV}, \quad (\text{II}) \\ \text{CN}(\widetilde{X}\,^2\Sigma^+) + \text{N}(^4S) & \Delta H_{\text{rxn,0}} = 4.563 \pm 0.050\,\text{eV}. \quad (\text{III}) \end{cases}$$

The above heats of reaction (at 0 K) represent a refinement of previous values and were determined directly from this work (see below).

All three channels are accessible following excitation of the 1_0^n, $n \geq 4$ transitions in Fig. 3. For each dissociation event, the photofragment mass ratios are calculated from the relative recoil distance of the coincident photofragments from the center of the neutral beam. This enables us to largely but not completely distinguish $\text{C} + \text{N}_2$ from $\text{N} + \text{CN}$ products, since our product mass resolution is only ~ 10. For data collected at a 1 m flight length, the $\widetilde{B} \leftarrow \widetilde{X}$ transitions with photon energies less than 5.1 eV produce a mass ratio of 12:28, indicating $\text{C} + \text{N}_2$ products. The observed mass distribution is significantly broadened at translational energies less than 0.7 eV for the 1_0^9 transition, implying that the $\text{N} + \text{CN}$ channel contributes at low E_T. Increasing the flight length to 2 m improves the detection efficiency of low translational energy fragments. At this flight length, the 1_0^6 and 1_0^7 transitions exhibit a photofragment mass ratio of 14:26 ($\text{N} + \text{CN}$) at translational energies < 0.3 and < 0.45 eV, respectively and a mass ratio of 12:28 at higher translational energies, as shown in Fig. 6. The photofragment mass ratio is 12:28 for the $\widetilde{c}\,^1\Pi_u \leftarrow \widetilde{a}\,^1\Delta_g$ and $\widetilde{d}\,^1\Delta_u \leftarrow \widetilde{a}\,^1\Delta_g$ transitions at all E_T.

$P(E_T)$ distributions for the $\text{C} + \text{N}_2$ channel from several $\widetilde{B} \leftarrow \widetilde{X}$ transitions are shown in Fig. 7; these distributions were taken at a flight length of 1 m. The distributions display a sharp onset at high translational energy and well-resolved structure with peaks separated by approximately 290 meV, corresponding to excitation of the N_2 product vibration. The full width at half maximum (FWHM) of each peak is approximately 150 meV with an asymmetric tail extending toward low translational energy. The assignment of the structure of the $P(E_T)$ distributions is presented in Sec. IV with
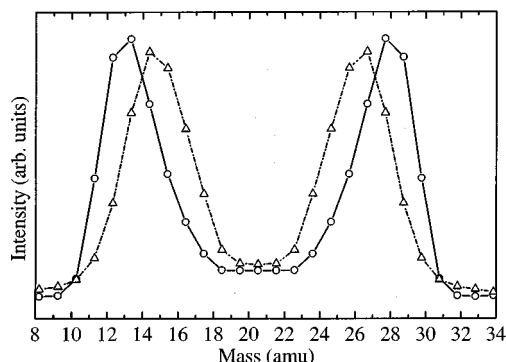
the resulting N_2 vibrational distributions listed in Table II. While the $P(E_T)$ distributions show highly structured features at high translational energy, the low kinetic energy regions ($E_T < 0.8$ eV) of these spectra are relatively broad and unresolved.

From our product mass analysis, of which Fig. 6 is an example, we expect significant $\text{N} + \text{CN}$ contributions at low E_T for the 1_0^n, $n \geq 6$ $\widetilde{B} \leftarrow \widetilde{X}$ transitions. The $\text{N} + \text{CN}$ $P(E_T)$ distributions for the low E_T regions of the 1_0^6, 1_0^7, and 1_0^9 transitions (the first two are from data at a flight length of 2 m) are shown in Fig. 8. The 1_0^6, 1_0^7, and 1_0^9 transitions yield $P(E_T)$ distributions with sharp narrow peaks (FWHM ≈ 100 meV) with maxima located at 0.19, 0.31, and 0.56 eV, respectively. The peak positions shift with increased excitation energy; consistent with opening of the $\text{N}(^4S) + \text{CN}(\widetilde{X}\,^2\Sigma^+)$ channel. The $P(E_T)$ distributions for the 1_0^7 and 1_0^9 transitions display additional peaks at ≈ 250 meV lower E_T; these are attributed to vibrational excitation of the CN fragment. There is signal extending to higher translational energies than energetically accessible for $\text{N} + \text{CN}$ products. This is caused by our limited photofragment mass resolution that cannot completely exclude $\text{N}_2 + \text{C}$ events from the $\text{N} + \text{CN}$ distribution.

The $\text{N} + \text{CN}$ photofragments have relatively low recoil energies (< 0.6 eV) and are therefore preferentially detected
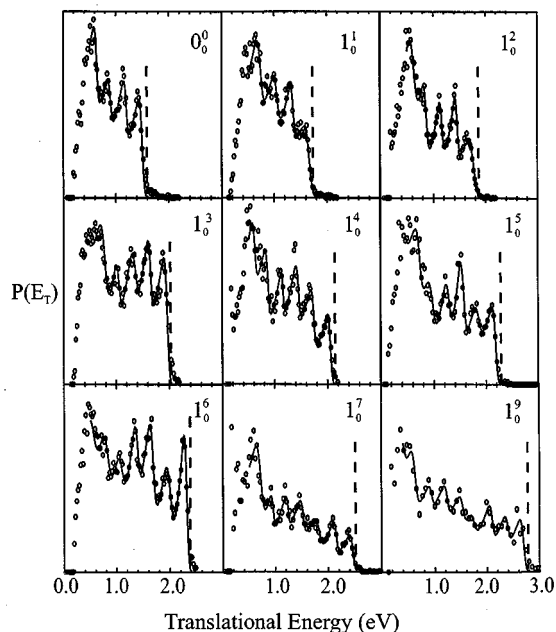

FIG. 6. Fragment mass distribution for $E_T < 0.35$ eV for the 1_0^7 transition (open circles) and $E_T > 0.5$ for the 1_0^6 transition (open triangles). The data was collected with a 2 m flight length.

FIG. 7. $P(E_T)$ distributions for the $\text{N}_2 + \text{C}(^3P)$ channel resulting from $\widetilde{B}\,^3\Sigma_u^- \leftarrow \widetilde{X}\,^3\Sigma_g^-$ transitions. The dashed vertical lines denote $E_T^{\max}$ for products. Data are shown with open circles, while the results of a fit to the product internal energy distribution are shown with a solid line.

TABLE II. Vibrational distributions of the N_2 and CN photofragments obtained from a fit of the $P(E_T)$ distributions, Figs.7–10, resulting from excitation of $\tilde{B}\,^3\Sigma_u^- \leftarrow \tilde{X}\,^3\Sigma_g^-$, $\tilde{d}\,^1\Delta_u \leftarrow \tilde{a}\,^1\Delta_g$, and $\tilde{c}\,^1\Pi_u \leftarrow \tilde{a}\,^1\Delta_g$ transitions of NCN,

Transition	Photon Energy (eV)	N_2 vibrational distributon							CN vibrational distribution	
		$v=0$ (%)	$v=1$ (%)	$v=2$ (%)	$v=3$ (%)	$v=4$ (%)	$v=5$ (%)	$v=6$ (%)	$v=0$ (%)	$v=1$ (%)
$\tilde{B}\,^3\Sigma_u^- \leftarrow \tilde{X}\,^3\Sigma_g^-$										
0_0^0	4.153	22	22	26	30					
1_0^1	4.283	22	19	31	28					
1_0^2	4.414	22	13	13	30	12				
1_0^3	4.542	26	20	12	12	24	6			
1_0^4	4.670	11	17	12	12	33	15			
1_0^5	4.790	15	9	9	9	24	32			
1_0^6	4.927	15	11	16	10	17	18	12	100	$\cdots$
1_0^7	5.049	9	10	14	12	12	13	30	60	40
1_0^9	5.299	14	12	14	9	19	17	15	60	40
$\tilde{d}\,^1\Delta_u \leftarrow \tilde{a}\,^1\Delta_g$										
c	4.646	18	16	17	14	21	14			
$\tilde{c}\,^1\Pi_u \leftarrow \tilde{a}\,^1\Delta_g$										
0_0^0	3.725	17	19	17	10	22	15			
2_1^1	3.735	13	12	19	17	19	20			

over the more energetic N_2+C products when a 2 m flight distance is used, preventing a precise determination of the branching ratio. By including the relative detector acceptances for the two product channels at both 1 and 2 m flight lengths, we estimate the relative yield of the CN+N channel for the 1_0^6, 1_0^7, and 1_0^9 transitions to be $\approx 25 \pm 10\%$.
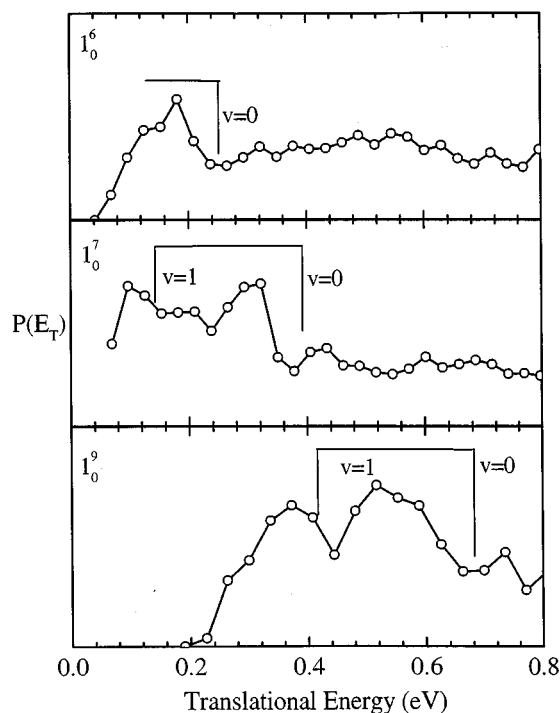
We have also obtained $P(E_T)$ distributions for $\tilde{c}\,^1\Pi_u \leftarrow \tilde{a}\,^1\Delta_g$ and $\tilde{d}\,^1\Delta_u \leftarrow \tilde{a}\,^1\Delta_g$ transitions. The $P(E_T)$ distribution resulting from the $\tilde{c}\,^1\Pi_u \leftarrow \tilde{a}\,^1\Delta_g$ (000–000) transition at a photon energy of 3.725 eV is shown in Fig. 9. At this photon energy, the maximum translational energy (E_T^{max}) is 2.19 and 0.93 eV for $C(^3P)$ and $C(^1D)$ products, respectively. These values are indicated by the dashed vertical lines. The onset for dissociation clearly occurs near 2.19 eV indicating that spin-forbidden triplet products are the primary photodissociation products. The $P(E_T)$ distribution is remarkably similar to the $\tilde{B} \leftarrow \tilde{X}$ transitions, showing resolved structure at high E_T with peak spacing of ≈ 290 meV and a FWHM of ≈ 150 meV while the distribution is significantly less structured for $E_T < 0.8$ eV. It is not obvious from the distribution if $C(^1D)$ products are present. However, the
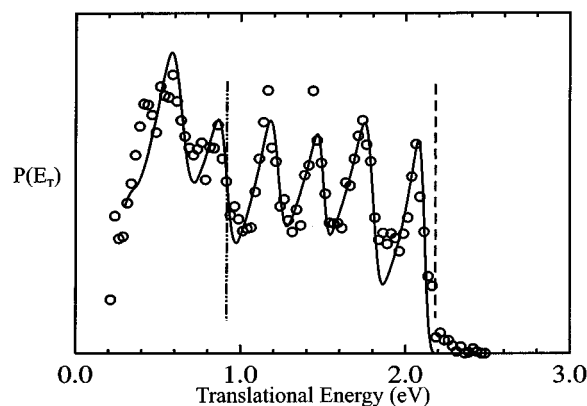

FIG. 8. $P(E_T)$ distributions analyzed with a 14:26 mass ratio for the 1_0^6, 1_0^7, and 1_0^9 transitions of the $\tilde{B}\,^3\Sigma_u^- \leftarrow \tilde{X}\,^3\Sigma_g^-$ band. The distributions for the 1_0^6 and 1_0^7 transitions were collected using a 2 m flight distance between the dissociation laser and the detector while a 1 m flight length was used for the 1_0^9 transition.

FIG. 9. $P(E_T)$ distribution for N_2+C products from the $\tilde{c}\,^1\Pi_u \leftarrow \tilde{a}\,^1\Delta_g$ 000–000 band. The two dashed vertical lines (———) and (-- - --) denote E_T^{max} for $C(^3P)$ and $C(^1D)$ products, respectively. Data are shown with open circles, while the results of a fit to the product internal energy distribution are shown with a solid line.
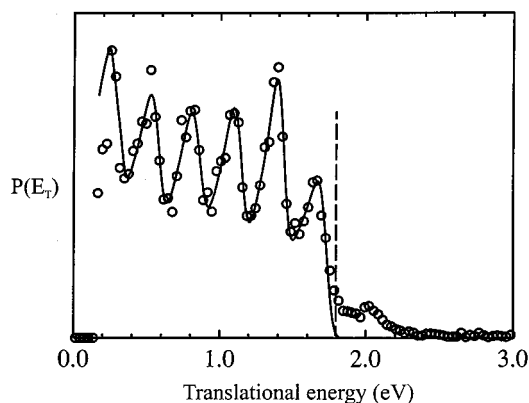
FIG. 10. $P(E_T)$ distribution for N_2+C products from a $\tilde{d}\,^1\Delta_u \leftarrow \tilde{a}\,^1\Delta_g$ transition at 37,476 cm^{-1}. Data are shown with open circles, while the results of a fit to the product internal energy distribution are shown with a solid line. The dashed vertical line represents $E_T^{\max}$ for C(^1D) products.

relative intensities of features with $E_T>0.9$ eV are similar to those for $E_T<0.9$ eV, indicating that the C(^1D) products are at best a minor channel; this point is revisited in Sec. IV.

Excitation of the (010–010) $^1\Delta_g \leftarrow {}^1\Phi_u$ transition yields a $P(E_T)$ distribution (not shown) which is very similar to that observed for the (000–000) transition, in that there is a structured progression of ≈ 290 meV for $E_T>0.8$ eV which becomes less structured for $E_T<0.8$ eV. The FWHM of the structured features are ≈ 180 meV, somewhat broader than those for the (000–000) transition. There does not appear to be any significant difference in the C(^1D):C(^3P) product branching ratios for the two transitions.

The $P(E_T)$ distribution for the $\tilde{d}\,^1\Delta_u \leftarrow \tilde{a}\,^1\Delta_g$ transition at an excitation energy of 4.646 eV is shown in Fig. 10. The singlet–triplet splitting, $E(\tilde{a}\,^1\Delta_g - \tilde{X}\,^3\Sigma_g^-)$, is 1.010 ± 0.010 eV.[18] Thus, the total energy of the radical above the ground electronic state after excitation is 5.656 eV with expected $E_T^{\max}$ values of 3.12 and 1.86 for C(^3P) and C(^1D) products, respectively. The onset for dissociation occurs near 1.8 eV indicating that the C(^1D)$+N_2$ products are the dominant channel. A small fraction ($<5\%$) of the total signal appears at translational energies greater than 1.8 eV. This feature is attributed to a hot band absorption from the $\tilde{X}$ state which dissociates to C(^3P)$+N_2$. The general features of the $P(E_T)$ distribution are similar to those for the $\tilde{B}\leftarrow\tilde{X}$ band. The distribution is highly structured with a peak spacing of approximately 290 meV and a FWHM of about 150 meV. However, in contrast to the $P(E_T)$ distributions for the $\tilde{B}\leftarrow\tilde{X}$ and $\tilde{c}\leftarrow\tilde{a}$ transitions, the $P(E_T)$ distribution for the $\tilde{d}\leftarrow\tilde{a}$ transition exhibits resolved structure at translational energies as low as 0.2 eV. It is worth emphasizing here that although the N(^4S)$+$CN($\tilde{X}\,^2\Sigma^+$) channel is energetically accessible by more than 1 eV, only a 12:28 mass ratio was observed for the photofragments.

The photofragment angular distributions are described by Eq. (1):[41]

$$I(\theta)=1/(4\pi)[1+P_2(\cos\theta)]. \tag{1}$$

The anisotropy parameter, β, can range from $+2$ to -1, corresponding to $\cos^2\theta$ and $\sin^2\theta$ distributions, respectively. The angular distributions for the N_2+C product channel for all three electronic transitions were found to be nearly isotropic with $\beta\approx 0$, while the N$+$CN channel was found to have an anisotropic angular distribution with $\beta=0.9$. The positive β parameter is consistent with the expected parallel transition dipole moment for the $\tilde{B}\,^3\Sigma_u^- \leftarrow \tilde{X}\,^3\Sigma_g^-$ band.

IV. ANALYSIS

The $P(E_T)$ distributions in Figs. 7–10 demonstrate how the excess energy above the dissociation threshold is distributed between the photofragments. The energy balance for NCN photodissociation to N_2+C is described by Eq. (2),

$$h\nu+E_{\text{int}}(\text{NCN})+E_{\text{elec}}(\text{NCN})$$
$$=D_0(\text{NCN})+E_T+E_v(N_2)+E_R(N_2)+E_{\text{elec}}(\text{C}), \tag{2}$$

where $h\nu$ is the photon energy, $E_{\text{int}}(\text{NCN})$ is the average rotational energy of the parent radical, $E_{\text{elec}}(\text{NCN})$ is the initial electronic state of the radical, D_0 is the dissociation energy, E_T is the measured translational energy, $E_v(N_2)$ and $E_R(N_2)$ are the N_2 vibrational and rotational energies, respectively, and $E_{\text{elec}}(\text{C})$ is the atomic state of carbon. An analogous equation can be written for the CN$+$N channel. The parent rotational temperature of 50 K yields $E_{\text{int}}(\text{NCN}) \approx 33$ cm^{-1}. $D_0(\text{NCN})$ for the N_2 loss channel can be extracted from these distributions by determining $E_T^{\max}$, the translational energy corresponding to photofragments with zero internal energy.

Although $E_T^{\max}$ is not always obvious from a $P(E_T)$ distribution, it can be readily determined from the distributions in Fig. 7 from the steep falloff in intensity toward the high energy side marked by the vertical dashed lines for each photon energy. Each $P(E_T)$ distribution then provides an independent measurement of D_0, all of which agree within our experimental resolution of 30 meV. An average of all of these values yields $D_0=2.54\pm 0.03$ eV and $\Delta H_{f,0\,K}(\text{NCN}) =4.83\pm 0.03$ eV. The latter agrees with the values of 4.89 ± 0.22 eV and 4.69 ± 0.13 eV from JANAF thermochemical tables[42] and recent *ab initio* calculations,[17] respectively, but our error bar is smaller. Contamination of the $P(E_T)$ distributions for the CN$+$N channel by N_2+C products prevents an exact measurement of $E_T^{\max}$ for the CN$+$N channel directly from the $P(E_T)$ distribution. From our experimentally determined $\Delta H_{f,0\,K}(\text{NCN})$ and literature values for $\Delta H_{f,0\,K}(\text{CN})=4.51\pm 0.02$ eV (Ref. 43) and $\Delta H_{f,0\,K}(\text{N}(^4S))=4.8796\pm 0.0010$ eV,[42] we calculate $D_0(\text{N–CN})=4.56\pm 0.04$ eV.

The $P(E_T)$ distributions for C$+N_2$ products and the N$+$CN products exhibit resolved structure corresponding to the vibrational excitation of the molecular fragment. In an attempt to determine the vibrational distribution of the diatomic fragment, we have fit each $P(E_T)$ distribution to a series of distribution functions f_v separated by the vibronic energy levels of the diatomic fragment (N_2 or CN)[44] with the total distribution given by Eq. (3):

$$F(E_T) = \sum_{v=0}^{v'} \alpha_v f_v [E_T - (h\nu - v\omega_2 - D_0 - \Delta), T, \delta]. \quad (3)$$

The individual distribution functions, f_v, are Gaussians convoluted with a Boltzmann distribution. The offset Δ and rotational temperature T were adjusted to fit the peak and width of each vibrational feature. Attempts to model the $P(E_T)$ distributions with a single rotational temperature for each vibrational product state proved less successful. The $P(E_T)$ distributions C+N_2 mass channel for the $\tilde{B}\,^3\Sigma_u^-$ $\leftarrow\tilde{X}\,^3\Sigma_g^-$ transition was fit with the C(^3P) products while the $\tilde{c}\,^1\Pi_u\leftarrow\tilde{a}\,^1\Delta_g$ transitions were fit with both C(^3P) and C(^1D) products. No substantial improvement to the fit was obtained by including the C(^1D) products. We estimate that the C(^1D) products comprise $\leqslant$10% of the total photodissociation signal. The $\tilde{d}\,^1\Delta_u\leftarrow\tilde{a}\,^1\Delta_g$ transition was fit using C(^1D) products exclusively.

The vibrational distributions for the $\tilde{B}\leftarrow\tilde{X}$ transitions, Table II, do not reveal any clear trends regarding the extent of vibrational excitation for the N_2 fragment as a function of excitation energy. There also does not appear to be any significant difference in the vibrational distributions resulting from the different NCN excited electronic states. The $P(E_T)$ distributions for the 1_0^7 and 1_0^9 transitions show population of both the $v=0$ and $v=1$ states of the CN fragment with an intensity ratio $v=0:v=1$ of $\approx$3:2.

We have also extracted the rotational distribution of the molecular fragment for each product vibrational state. The offset Δ and rotational temperature T in Eq. (3) are used to determine N_{peak}, the rotational quantum number corresponding to the peak of each distribution, f_v. A unique N_{peak} value for each N_2 product vibrational state is then obtained for every $P(E_T)$ distribution. The $P(E_T)$ distributions for the 1_0^n $\tilde{B}\leftarrow\tilde{X}$ transitions yield very similar N_{peak} values ($\pm$3 quanta) for the same N_2 product vibrational state (i.e., N_{peak} is independent of n). However, the N_{peak} values exhibit a pronounced dependence on the vibrational quantum number of the N_2 fragment.

In Fig. 11, the average N_{peak} values for the 1_0^n $\tilde{B}\leftarrow\tilde{X}$ transitions for each N_2 product state are plotted versus the N_2 vibrational quantum number; the N_{peak} values for the $\tilde{c}\,^1\Pi_u$ $\leftarrow\tilde{a}\,^1\Delta_g$ (000–000) and $\tilde{d}\,^1\Delta_u\leftarrow\tilde{a}\,^1\Delta_g$ transitions are also shown. For all three transitions, the N_2 fragment displays substantial rotational excitation with distributions peaking between 20–40 quanta of rotation depending on the vibrational quantum number of the fragment and the initial electronic transition. The N_{peak} values for the $\tilde{B}\,^3\Sigma_u^-$ and $\tilde{c}\,^1\Pi_u$ states increase substantially for higher vibrational states of the N_2 fragment, while the N_{peak} values for the $\tilde{d}\,^1\Delta_u$ state are generally lower than for the other two states and vary much less with N_2 vibrational state. The CN photofragment was found to have a rotational distribution described by a Boltzmann temperature of 700 K with $N_{peak}\approx10$.

V. DISCUSSION

The product state energy distributions for the fragmentation of NCN reveal that complicated dynamics are in-
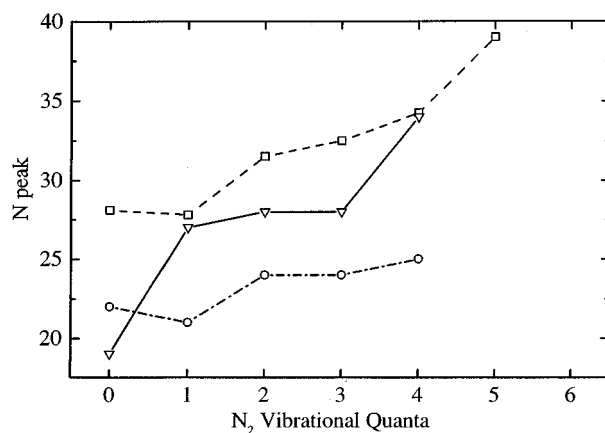

FIG. 11. The average N_{peak} values for all the 1_0^n $\tilde{B}\leftarrow\tilde{X}$ transitions in Fig. 7 (squares), as well as the N_{peak} values for the $\tilde{c}\,^1\Pi_u\leftarrow\tilde{a}\,^1\Delta_g$ origin (triangles) and transition c of the $\tilde{d}\,^1\Delta_u\leftarrow\tilde{a}\,^1\Delta_g$ band (circles) are plotted versus the N_2 vibrational quantum number.

volved in the dissociation of this triatomic radical. The $\tilde{B}\,^3\Sigma_u^-$ state yields N_2+C(^3P) products at all photon energies explored. At photon energies greater than 4.9 eV, the $\tilde{B}\,^3\Sigma_u^-$ state also produces CN($\tilde{X}\,^2\Sigma^+$)+N(^4S) products as a minor channel $\approx$25$\pm$10%. C(^3P) products are the dominant dissociation channel ($\geqslant$90%) for the $\tilde{c}\,^1\Pi_u$ state even though C(^1D) products are energetically available by more than 1.8 eV, while the $\tilde{d}\,^1\Delta_u$ state dissociates to C(^1D) products exclusively. The $\tilde{B}\,^3\Sigma_u^-$ and $\tilde{c}\,^1\Pi_u$ states possess very similar $P(E_T)$ distributions with well resolved vibrational features for $E_T>0.8$ eV and broad unresolved structure at lower translational energies. The $\tilde{d}\,^1\Delta_u$ state in comparison exhibits resolved vibrational structure for translational energies as low as 0.2 eV. Finally, the CN fragment is produced with substantially less rotational excitation ($N_{peak}=10$) than the N_2 photofragment ($N_{peak}=20$–40), implying that the mechanisms for these two dissociation channels are distinct.

The ground and all excited electronic states accessed in this study are linear, but the dominance of C+N_2 photoproducts indicates that the photodissociation mechanism must involve cyclic and/or bent states. The extensive vibrational and rotational excitation of the N_2 product are also consistent with dissociation through a bent or cyclic state with the N–N bond forming and C–N bonds breaking at large N–N distances leading to an extended vibrational progression in the N_2 photoproduct. Rotational excitation of the N_2 fragment is generated from parent molecular rotation and from the torque applied at the transition state. The trend of increasing rotational excitation with N_2 vibrational quantum number for the $\tilde{B}\,^3\Sigma_u^-$ and $\tilde{c}\,^1\Pi_u$ states is similar to that seen by Continetti et al.[32] for the photodissociation of N_3 and by Zare and co-workers[45] for the photodissociation of ICN.

Formation of product from the two end atoms of a triatomic, particularly a linear one, is relatively uncommon as it requires a low energy cyclic (or at least strongly bent) transition state. Such a transition state has been proposed in the photodecomposition of OClO which yields the lowest energy products, O_2+Cl, as a minor channel ($\leqslant$4%).[46–48] The larg-

est relative yields of this channel result from excitation of the bend and symmetric stretch modes, implying a concerted dissociation involving a transition state of approximately C_{2v} symmetry. *Ab initio* calculations[49–53] for O_3 have located minima for ring structures of D_{3h} symmetry, however, the poor Franck–Condon overlap with the ground state and a large barrier to dissociation via C_{2v} symmetry suggests that this pathway does not contribute. The dissociative ionization of CS_2 yields S_2^+ as minor channel (<9%) from the decay of the linear excited states of CS_2^+.[54,55] The translational energy distributions of the S_2^+ ion[56] are structureless single peaks with only 10%–26% of the available energy projected into translation indicating extensive vibrational and rotational excitation of the S_2^+ fragment, consistent with a dissociation pathway involving a cyclic intermediate.

Martin *et al.*[24] have performed *ab initio* calculations for linear, bent, and cyclic structures for NCN and CNN. Their calculations within the C_{2v} point group have located a local minimum with $^3A_2$ symmetry and a transition state with $^3B_1$ symmetry at 3.01 and 4.76 eV, respectively, above the linear ground state of NCN. As shown in Fig. 1, the $\tilde{A}\,^3\Pi_u$ state adiabatically correlates to the $^3B_1$ state while the $\tilde{B}\,^3\Sigma_u^-$ state correlates to the lower lying $^3A_2$ state. Both the $^3A_2$ and $^3B_1$ states correlate to ground state products in C_{2v} symmetry. If we assume that the dissociation proceeds via C_{2v} symmetry, then the $\tilde{A}\,^3\Pi_u$ state cannot dissociate since it does not correlate to the lower energy $^3A_2$ state and does not have enough energy to access the $^3B_1$ state. On the other hand, the $\tilde{B}\,^3\Sigma_u^-$ state has a relatively low energy pathway through a cyclic transition state to $C(^3P)+N_2$ products. This simple picture therefore explains why only the $\tilde{B}\,^3\Sigma_u^-$ state dissociates, even though both states lie above the $C+N_2$ asymptote. Furthermore, the calculations predict a N–N bond distance of 1.737 Å for the $^3A_2$ state, consistent with the extensive vibrational excitation of the N_2 photofragment (R_e =1.098 Å).

Martin *et al.* also found a less symmetric $^3A''(C_s)$ transition state through uphill following of the bending mode of CNN. This state lies slightly lower in energy than the $\tilde{A}\,^3\Pi_u$ state, but the absence of $\tilde{A}\,^3\Pi_u$ state dissociation suggests that this transition state does not play a role in the dissociation dynamics.

We next consider the dissociation mechanism of the $\tilde{c}\,^1\Pi_u$ state. Martin *et al.* report only one singlet minimum energy structure with symmetry $^1A_1$ located 1.57 eV above the ground state, which correlates adiabatically with the $\tilde{c}\,^1\Pi_u$ state. However, since spin-forbidden $C(^3P)$ products are clearly the dominant dissociation channel from the $\tilde{c}\,^1\Pi_u$ state, it is unlikely that this structure is involved in the dissociation mechanism. The $C(^3P):C(^1D)$ branching ratio does not appear to change significantly for the (010–010) $^1\Delta_g \leftarrow {}^1\Phi_u$ transition suggesting that this upper state is also not strongly coupled to the $^1A_1$ state.

The formation of $C(^3P)$ products from the $\tilde{c}\,^1\Pi_u$ state clearly indicates that the dissociation mechanism involves intersystem crossing to a triplet surface. The $P(E_T)$ distributions for the $\tilde{B}\,^3\Sigma_u^-$ and $\tilde{c}\,^1\Pi_u$ states are noticeably similar with both displaying an increase in rotational excitation with

increased vibrational excitation. The $\tilde{c}\,^1\Pi_u$ state has been rotationally resolved by Kroto[7] with an instrument resolution of 0.1 cm^{-1} and appears to be instrument limited, indicating that the lifetime of the $\tilde{c}\,^1\Pi_u$ state is >50 ps. The long lifetime, spin-forbidden products, and $P(E_T)$ distribution suggest that the $\tilde{c}\,^1\Pi_u$ state first intersystem crosses to the $\tilde{B}\,^3\Sigma_u^-$ state prior to dissociation.

The $\tilde{d}\,^1\Delta_u$ state, in contrast to the $\tilde{c}\,^1\Pi_u$ state, leads to spin-allowed $C(^1D)$ dissociation products. Although the $N(^4S)+CN(\tilde{X}\,^2\Sigma^+)$ products are energetically accessible by 1.08 eV, these spin-forbidden products are not observed. The $P(E_T)$ distribution which results from excitation to the $\tilde{d}\,^1\Delta_u$ state, Fig. 8, exhibits an extended vibrational progression of the N_2 photofragment. However, Fig. 11 shows that the degree of N_2 rotational excitation is lower for $\tilde{d}\,^1\Delta_u$ dissociation than for $\tilde{B}\,^3\Sigma_u^-$ or $\tilde{c}\,^1\Pi_u$ state dissociation. In addition, the rotational excitation of the N_2 fragment is approximately the same for all N_2 vibrational states, in contrast to the $\tilde{B}\,^3\Sigma_u^-$ and $\tilde{c}\,^1\Pi_u$ states. It therefore appears that the triplet and singlet surfaces have different topologies.

In NCN predissociation, the N_2 rotational distribution is determined largely by the energy and geometry of the transition state, and by the torque exerted on the N_2 in the exit channel. The lower rotational excitation for $C(^1D)+N_2$ products can therefore be attributed to a number of factors. The experiments of Milligan and Jacox[11] indicate that that $C(^1D)$ atoms react readily in a nitrogen matrix to form NCN while $C(^3P)$ atoms do not, implying that the $C(^1D)$ dissociation products do not have a barrier to recombination, while a substantial barrier exists for the triplet channel. This is consistent with the extensive work on reactions of atomic oxygen, in which $O(^1D)$ but not $O(^3P)$ is known to undergo a variety of insertion reactions with no barrier.[57] However, one must be careful in applying these considerations to our experiment, because recombination presumably occurs on the lowest energy singlet or triplet surface of NCN whereas the dissociation dynamics in our experiment are launched from an electronically excited state.

While the dominant photodissociation products observed in this study are N_2+C, the $CN+N$ channel is observed from the $\tilde{B}\,^3\Sigma_u^-$ state at photon energies >4.9 eV. Both the $CN(v=0)$ and vibrationally excited $CN(v=1)$ products are observed, consistent with an expected large change in CN bond distance from the $\tilde{B}\,^3\Sigma_u^-$ state of the NCN radical to the $CN(\tilde{X}\,^2\Sigma^+)$ fragment. The rotational distribution peaks at $N=10$, a value less than half that observed for the N_2 loss channels. The limited rotational excitation and positive photofragment anisotropy, $\beta=0.9$, are consistent with a linear dissociation pathway. Freysinger *et al.*[58] have examined the diabatic and adiabatic electronic correlations for the linear states of isoelectronic N_3^+ ion into products N^++N_2 and N_2^++N,[58] which are isoelectronic with the $C+N_2$ and $N+CN$ products observed in this study. The $\tilde{B}\,^3\Sigma_u^-$ state correlates adiabatically to $N(^4S)+CN(\tilde{X}\,^2\Sigma^+)$ and correlates diabatically to the higher energy products $N(^2D)$ $+CN(\tilde{A}\,^2\Pi)$, while the $N(^4S)+CN(\tilde{X}\,^2\Sigma^+)$ products correlate diabatically to a higher-lying $^3\Sigma_u^-$ state. The crossing of

these two diabatic surface will likely produce a conical intersection leading to a barrier to dissociation along the adiabatic surface. The CN+N channel is first observed at photon energies which exceed $D_0(N-CN)$ by more than 0.39 eV providing an upper limit for the barrier height.

It is surprising that the CN+N channel, which appears to dissociate via a linear pathway, does not become the dominant channel once it is energetically accessible, comprising only $25\pm10\%$ of the total dissociation signal. The dominance of the $N_2+C(^3P)$ channel is further proof that the coupling of the $\widetilde{B}\,^3\Sigma_u^-$ state to bent or cyclic states is highly efficient.

VI. CONCLUSIONS

The photodissociation dynamics of the $\widetilde{B}\,^3\Sigma_u^-$, $\widetilde{c}\,^1\Pi_u$, and $\widetilde{d}\,^1\Delta_u$ states of NCN radical have been investigated by fast beam photofragment spectroscopy. Both the $\widetilde{B}\,^3\Sigma_u^-$ and $\widetilde{c}\,^1\Pi_u$ states photodissociate to ground state products $N_2+C(^3P)$ while the $\widetilde{d}\,^1\Delta_u$ state dissociates to $N_2+C(^1D)$. Based on the identity of the products, one expects dissociation to occur through a cyclic or strongly bent transition state; this is consistent with the extensive vibrational and rotational excitation of the N_2 photoproduct from all three states. For the $\widetilde{B}\,^3\Sigma_u^-$ and $\widetilde{c}\,^1\Pi_u$ states, the rotational excitation appears to increase with vibrational excitation. The similarity in the $P(E_T)$ distributions and the production of the same photoproducts for the $\widetilde{B}\,^3\Sigma_u^-$ and $\widetilde{c}\,^1\Pi_u$ states suggest that the two states dissociate along the same surface, requiring that the $\widetilde{c}\,^1\Pi_u$ state undergoes intersystem crossing to the $\widetilde{B}\,^3\Sigma_u^-$ state prior to dissociation.

Finally, the CN+N product channel was observed from the $\widetilde{B}\,^3\Sigma_u^-$ state for photon energies greater than 4.9 eV comprising $\approx25\pm10\%$ of the total dissociation signal. The rotational distribution and anisotropic angular distribution, $\beta=0.9$, suggests that these photoproducts are formed via a linear dissociation pathway.

ACKNOWLEDGMENTS

[1] L. J. Butler and D. M. Neumark, J. Phys. Chem. **100**, 12801 (1996).

[2] K. R. Jennings and J. W. Linnett, Trans. Faraday Soc. **56**, 1737 (1960).

[3] G. P. Smith, R. A. Copeland, and D. R. Crosley, J. Chem. Phys. **91**, 1987 (1989).

[4] C. R. O'Dell, C. O. Miller, A. L. Cochran, W. D. Cochran, C. B. Opal, and E. S. Barker, Astrophys. J. **368**, 616 (1991).

[5] A. D. Walsh, J. Chem. Soc. **1953**, 2266.

[6] G. Herzberg and D. N. Travis, Can. J. Phys. **42**, 1658 (1964).

[7] H. W. Kroto, Can. J. Phys. **45**, 1439 (1967).

[8] H. W. Kroto, J. Chem. Phys. **44**, 831 (1966).

[9] H. W. Kroto, T. F. Morgan, and H. H. Sheena, Trans. Faraday Soc. **66**, 2237 (1970).

[10] D. E. Milligan, M. E. Jacox, and A. M. Bass, J. Chem. Phys. **43**, 3149 (1965).

[11] D. E. Milligan and M. E. Jacox, J. Chem. Phys. **45**, 1387 (1966).

[12] D. McNaughton, G. F. Metha, and R. Tay, Chem. Phys. **198**, 107 (1995).

[13] S. A. Beaton, Y. Ito, and J. M. Brown, J. Mol. Spectrosc. **178**, 99 (1996).

[14] S. A. Beaton and J. M. Brown, J. Mol. Spectrosc. **183**, 347 (1997).

[15] K. D. Hensel and J. M. Brown, J. Mol. Spectrosc. **180**, 170 (1996).

[16] M. Wienkoop, W. Urban, and J. M. Brown, J. Mol. Spectrosc. **185**, 185 (1997).

[17] E. P. Clifford, P. G. Wenthold, W. C. Lineberger, G. A. Petersson, and G. B. Ellison, J. Phys. Chem. A **101**, 4338 (1997).

[18] T. R. Taylor, R. T. Bise, K. R. Asmis, and D. M. Neumark, Chem. Phys. Lett. **301**, 413 (1999).

[19] Z. L. Cai, G. H. Sha, C. H. Zhang, and M. B. Huang, Theochem **85**, 303 (1992).

[20] G. Berthier and L. Kurdi, Acad. Sci., Paris, Ser. II (Mec., Phys., Chim., Sci. Univers. Sci. Terre) **299**, 1171 (1984).

[21] H. U. Suter, M. B. Huang, and B. Engels, J. Chem. Phys. **101**, 7686 (1994).

[22] C. Thomson, J. Chem. Phys. **58**, 841.

[23] G. R. Williams, Chem. Phys. Lett. **25**, 602 (1974).

[24] J. M. L. Martin, P. R. Taylor, J. P. Francois, and R. Gijbels, Chem. Phys. Lett. **226**, 475 (1994).

[25] V. E. Bondybey and J. H. English, J. Chem. Phys. **67**, 664 (1977).

[26] M. E. Jacox, J. Mol. Spectrosc. **72**, 26 (1978).

[27] T. D. Goldfarb and G. C. Pimentel, J. Am. Chem. Soc. **82**, 1865 (1959).

[28] M. C. Curtis, A. P. Levick, and P. J. Sarre, Laser Chem. **9**, 359 (1988).

[29] G. W. Robinson and M. McCarty, Jr., J. Am. Chem. Soc. **82**, 1859 (1960).

[30] E. Wasserman, L. Barash, and W. A. Yager, J. Am. Chem. Soc. **87**, 2075 (1965).

[31] H. Choi, D. H. Mordaunt, R. T. Bise, T. R. Taylor, and D. M. Neumark, J. Chem. Phys. **108**, 4070 (1998).

[32] R. E. Continetti, D. R. Cyr, D. L. Osborn, D. J. Leahy, and D. M. Neumark, J. Chem. Phys. **99**, 2616 (1993).

[33] D. J. Leahy, D. L. Osborn, D. R. Cyr, and D. M. Neumark, J. Chem. Phys. **103**, 2495 (1995).

[34] D. L. Osborn, H. Choi, D. H. Mordaunt, R. T. Bise, D. M. Neumark, and C. M. Rohlfing, J. Chem. Phys. **106**, 3049 (1997).

[35] D. L. Osborn, D. J. Leahy, D. R. Cyr, and D. M. Neumark, J. Chem. Phys. **104**, 5026 (1996).

[36] J. M. B. Bakker, J. Phys. E **6**, 785 (1973).

[37] J. M. B. Bakker, J. Phys. E **7**, 364 (1974).

[38] D. P. de Bruijn and J. Los, Rev. Sci. Instrum. **53**, 1020 (1982).

[39] R. E. Continetti, D. R. Cyr, D. L. Osborn, D. J. Leahy, and D. M. Neumark, J. Chem. Phys. **99**, 2616 (1993).

[40] This gas phase value for v'' is determined from $v'=1254$ cm^{-1} (Ref. 3) and $v'-v''=-5$ cm^{-1} (Ref. 6).

[41] R. N. Zare, Mol. Photochem. **4**, 1 (1972).

[42] M. W. Chase, Jr., C. A. Davies, J. R. Downey, Jr., D. J. Frurip, R. A. McDonald, and A. N. Syverud, J. Phys. Chem. Ref. Data Suppl. 1, **14** (1985).

[43] Y. Huang, S. A. Barts, and J. B. Halpern, J. Phys. Chem. **96**, 425 (1992).

[44] K. P. Huber and G. Herzberg, *Constants of Diatomic Molecules* (Van Nostrand Reinhold, New York, 1979).

[45] M. A. O'Halloran, H. Joswig, and R. N. Zare, J. Chem. Phys. **87**, 303 (1987).

[46] H. F. Davis and Y. T. Lee, J. Phys. Chem. **96**, 5681 (1992).

[47] E. Bishenden and D. J. Donaldson, J. Chem. Phys. **99**, 3129 (1993).

[48] E. Bishenden and D. J. Donaldson, J. Chem. Phys. **101**, 9565 (1994).

[49] S. Xantheas, G. J. Atchity, S. T. Elbert, and K. Ruedenberg, J. Chem. Phys. **94**, 8054 (1991).

[50] S. Xantheas, S. T. Elbert, and K. Ruedenberg, J. Chem. Phys. **93**, 7519 (1990).

[51] T. Muller, S. S. Xantheas, H. Daschel, R. J. Harrison, N. Jaroslaw, R. Shepard, G. S. Kedziora, and H. Lischa, Chem. Phys. Lett. **293**, 72 (1998).

[52] A. Banichevich and S. D. Peyerimhoff, Chem. Phys. **174**, 93 (1993).

[53] M. Braunstein, P. J. Hay, R. L. Martin, and R. T Pack, J. Chem. Phys. **95**, 8239 (1991).

[54] B. Brehm, J. H. D. Eland, R. Frey, and A. Kustler, Int. J. Mass Spectrom. Ion Phys. **12**, 212 (1973).

[55] J. H. D. Eland and J. Berkowitz, J. Chem. Phys. **70**, 5151 (1979).

[56] M. Hamdan, F. M. Harris, and J. H. Beynon, Int. J. Mass Spectrom. Ion Processes **74**, 303 (1986).

[57] M. Alagia, N. Balucani, P. Casavecchia, D. Stranges, and G. G. Volpi, J. Chem. Soc., Faraday Trans. **91**, 575 (1995).

[58] W. Freysinger, F. A. Khan, P. B. Armentrout, P. Tosi, O. Dmitriev, and D. Bassi, J. Chem. Phys. **101**, 3688 (1994).